MOX-Report No. 34/2021

An efficient and robust soil erosion model at the basin scale

Bonaventura, L.; Gatti F.; Menafoglio A.; Rossi D.; Brambilla D.; Papini M.; Longoni L.

MOX, Dipartimento di Matematica
Politecnico di Milano, Via Bonardi 9 - 20133 Milano (Italy)

mox-dmat@polimi.it http://mox.polimi.it

An efficient and robust soil erosion model at the basin scale

Luca Bonaventura [(1)] Federico Gatti[(1)] Alessandra Menafoglio[(1)] Daniele Rossi[(1)]
Davide Brambilla[(2)] Monica Papini[(2)] Laura Longoni[(2)]

June 3, 2021

[(1)] MOX – Modelling and Scientific Computing
Dipartimento di Matematica, Politecnico di Milano
Piazza Leonardo da Vinci, 20133 Milano, Italy
luca.bonaventura@polimi.it
federico.gatti@polimi.it
alessandra.menafoglio@polimi.it

[(2)] Dipartimento di Ingegneria Civile e Ambientale
Politecnico di Milano
Via G. Previati 1/c, 23900 Lecco, Italy
davide.brambilla@polimi.it
monica.papini@polimi.it
laura.longoni@polimi.it

Keywords: basin scale modeling, erosion modeling, semi-implicit time discretization, finite differences, finite volumes.

AMS Subject Classification: 5L60, 35Q35, 65Z05, 76B03, 76D99

Abstract

We present a numerical model of soil erosion at the basin scale that allows one to describe surface run-off without *a priori* identifying drainage zones, river beds and other water bodies. The model is based on robust and unconditionally stable numerical techniques and guarantees mass conservation and positivity of the surface and subsurface water layers. Furthermore, the method is equipped with a geostatistical preprocessor that can perform downscaling of data retrieved from digital databases at coarser resolutions and integrate them with field measurements. Numerical experiments on both idealized and realistic configurations demonstrate the effectiveness of the proposed method in reproducing transient high resolution features at a reduced computational cost and to reproduce correctly the main hydrographic features of the considered catchment. Furthermore, probabilistic forecasts can be carried out, also with limited computational effort, based on soil data automatically generated by the geostatistical preprocessor. Even though the model results are still far from full quantitative agreement with the available data, robust estimates of water levels, discharge and of the order of magnitude of the total sediment yield were achieved in two validation experiments on realistic benchmarks.

1 Introduction

Soil erosion in mountain catchments is a widely studied phenomenon with major economical and societal impacts. A great number of models for the simulation of this phenomenon exist, see e.g., among many others, [25, 29, 30, 47, 53, 57] and the references therein. Even though a complete review of these models goes beyond the scope of this paper, a more detailed discussion of some of the most relevant conceptual and physically based models is the starting point of our work. One conclusion that can be anticipated is that most of the models available for high resolution simulation of soil erosion at the basin scale suffer from several basic shortcomings, such as the need for substantial pre-processing of the orography data and for *a priori* identification of river beds and other drainage zones.

Our goal in this work is to introduce a novel approach to the distributed modelling of soil erosion over mountain catchments which addresses some of these shortcomings. The main novel feature of the proposed model consists in the use of the De Saint-Venant equations to model surface water flow over the whole domain, without *a priori* identification of drainage zones. This allows one to model basins in which strong variations of the surface run-off occur without *ad hoc* hypotheses, as well as to include naturally lakes and other water reservoirs. The model is also equipped with a geostatistical preprocessor, fully described in [32], which can be used to downscale to fine resolution meshes the soil composition data available in global databases like SoilGrids [42] and to integrate them with field measurements. With respect to all the other model components, very simple choices have been made so far, which are justified for this first development stage and which are sufficient to demonstrate the model capabilities. However, all these choices can and should be revised in future development stages, depending essentially on the level of computational resources that are available to run the model. Several possible improvements will be already outlined in this work.

The model equations are approximated numerically using a very well tested, efficient and robust semi-implicit discretization method [13, 17]. The proposed technique yields an effective spatially distributed model, able to handle the wide range of transients that can arise in long term simulations and to run even at high resolution with time step values that are dictated by accuracy rather than stability reasons. Furthermore, a dynamical time step adaptation is employed, which automatically reduces the time step during intensive rainfall events and increases it when no precipitation occurs. The numerical discretization guarantees exact mass conservation, positivity of the water and sediment layers and consistency of the discretized equations for tracers with that for the water mass, according to the prescriptions in [36]. Preliminary versions of this model have been introduced in [1, 37]. The model has been implemented in an object oriented programming language.

The results of the first verification and validation experiments confirm the model efficiency, robustness and flexibility and demonstrate its potential role as the basis for a more comprehensive simulation tool with uncertainty quantification capabilities.

The structure of the paper is the following. A review of erosion models at the basin scale is presented in Section 2, where several shortcomings of the currently available models are highlighted. The governing equations of the proposed model are then introduced in Section 3, while their discretization is presented in Section 4. The data preprocessing strategy and the companion geostatistical preprocessor are briefly described in Section 5. A first attempt at verification and validation of the model is presented in Sections 6,7, concerning respectively simulations on idealized and realistic orography. Some conclusions and some perspectives for future developments are discussed in Section 8.

2 A review of erosion models at the basin scale

As already mentioned in Section 1, a complete review of soil erosion models at the basin scale goes beyond the scope of this paper. A well known attempt in this direction is represented by [53], while more recent efforts are presented in [25, 30, 47, 57], among many others.

Erosion models can broadly be classified as either empirical, conceptual or physically based. Empirical models describe the effects of erosion process (for example, the amount of detached soil) in terms of parameters that can either be measured, such as the temperature, slope gradient and basin area, or need to be subjectively assigned, such as the soil erodibility factor and the vegetation cover. These models do not seek to describe the underlying physics and assume homogeneity of input data throughout the basin. Therefore, they give more reliable results when applied to limited areas, where the variation of such parameters may be considered negligible. Examples of this group are the well known USLE [82], RUSLE [61] and the Gavrilović models [33, 34, 24].

Conceptual models usually represent catchments as a series of internal storage units and model the general mechanisms that govern the interchange of sediment and water between these storage compartments. Input parameters are usually obtained by calibration, based on field-measured data. Research shows that determining the optimal set of values can be cumbersome. In fact, there might be many sets of optimal parameter values and increasing the model complexity increases the difficulty in the determination of these values [53]. Among the best known conceptual models we mention for example AGNPS [83], SWRRB , [5], [81], LASCAM [77, 78], SEDEM [65]. All these models often use empirical models as subcomponents. For the purposes of the present work, the model presented in [8] is especially

relevant, since its formulation has represented the starting point of our development. However, the original approach of [8] does not guarantee mass conservation and has several limitations also common to other models, such as for example the need to identify *a priori* the drainage zones.

Physically based models are the most complex ones and try to simulate directly most of the processes that take place in reality, like the impact of raindrops on the soil and the consequent detachment of soil particles. These models usually rely on the numerical solution of the mass and momentum conservation equations for the water flow and of the mass conservation equation for sediments. These models require a large amount of input data, which are often scarce or inconsistent. This leads to poor input datasets that create errors in output, which can be seen as a drawback that generally applies to all the models of this group. Another problem is the risk of overparametrization. More specifically, the large number of parameters (tens or even hundreds) that these models require makes it almost impossible to find optimal values [53]. Although the parameters have physical meaning and should be measured in the field, this is sometimes impossible in practice due to their temporal and spatial variability and to time and budget limitations. As a result, either calibration or some form of uncertainty quantification have to be performed, thus reducing the effectiveness of the model predictions. Among these models, we can mention LISEM [66], WEPP [73], EUROSEM [56], SHESED [79] (which is based on the previous SHE hydrological model [2, 3]), DHSVM [80, 23], TOPKAPI [21, 70] and GEOTOP [64, 69, 26]. The latter, however, focuses more on evapotranspiration and energy budgets than on erosion modelling. While including rather sophisticated descriptions of soil erosion, all these models use simplified equations for the surface run-off, require *a priori* identification of rivers and drainage zones and are not capable of handling domains in which larger water bodies are present, such as lakes or estuaries.

3 The mathematical model

In this Section, we describe the governing equations that constitute the proposed basin scale model, which can be seen as an improvement and extension of the model proposed in [8], from which the general concept and some basic modelling choices for several physical processes are borrowed. On the other hand, the proposed approach is fully mass conservative and employs the De Saint-Venant equations to model surface water flow over the whole domain.

We consider a rectangular domain $\Omega = [0, L_x] \times [0, L_y]$ which contains a subdomain $\Omega_b \subset \Omega$ that represents the basin under study. This subdomain is usually identified by geometric and hydrologic considerations. We then consider the drainage subdomain $\Omega_d \subset \Omega_b$, whose extension varies in time and which is only implicitly defined as the portion of Ω_b where the depth

of the surface water layer H is above a minimum threshold H_d. Notice that $H = \eta - b$, where b denotes the orography profile defined on Ω and η is the height of water free surface. For $\mathbf{x} \in \Omega_d$, we model the motion of the surface water layer by the De Saint-Venant equations

$$\begin{aligned} \partial_t H + \nabla \cdot (H\mathbf{u}) &= (1-\mu)p - f, \\ \partial_t \mathbf{u} + \mathbf{u} \cdot \nabla \mathbf{u} &= -g\nabla\eta - \gamma(\mathbf{u})\mathbf{u}. \end{aligned} \tag{1}$$

Here $\mathbf{u}$ is the surface water velocity, g is the gravitational acceleration and γ is a friction term to be defined later. The source term p denotes the precipitation intensity, which is corrected to account for snow by the non-dimensional parameter μ. This parameter takes the value of 1 if the ground temperature is lower than or equal to the melting temperature T_m and 0 if it is higher. The infiltration term f, to be defined in the following, represents the exchange of water mass between the surface layer and the gravitational layer.

It is important to remark that the equation for the surface water layer thickness is in divergence form, which guarantees exact mass conservation if appropriate numerical methods are employed. We also assume that the orography profile is not changing in time, so that $\partial_t H = \partial_t \eta$. This simplification is justified in the limit of thin sediment layers, while bed evolution can be taken into account, if necessary, by a decoupled approach, see e.g. [31]. Notice also that, for $\mathbf{x} \in \Omega_b \backslash \Omega_d$, i.e. wherever $H \leq H_d$, the governing equations are instead modified by assuming zero horizontal velocities and, as a consequence, null mass fluxes, so that in this region one has

$$\begin{aligned} \partial_t H &= (1-\mu)p - f, \\ \mathbf{u} &= \mathbf{0}. \end{aligned} \tag{2}$$

In this way, drainage zones are automatically identified while preserving mass conservation. Notice that, on the portion of $\partial\Omega_d$ on which $\mathbf{u} = \mathbf{0}$, which coincides with the portion of $\partial\Omega_d$ which is in the interior of Ω_b, zero mass flux boundary conditions are naturally imposed. On the other hand, on $\partial\Omega_d \cap \partial\Omega_b$ outflow boundary conditions are assigned. Concerning the friction coefficient, it is defined by the Manning-Strickler formula

$$\gamma(\mathbf{u}) = \frac{g\, n^2}{H^{\frac{4}{3}}} \, |\mathbf{u}| \,, \tag{3}$$

where n is the Manning friction coefficient, see e.g. [18]. The appropriate model for this coefficient that is valid for steep slopes and mountain torrents has been discussed in the series of papers [20, 62, 63], where a number of corrections to the values typically employed in river hydraulics have been

proposed. Following [62], we will consider the formula

$$\begin{aligned}
\frac{1}{n_r} &= \frac{0.56\, g^{0.44}(H\,|\mathbf{u}|)^{0.11}}{|\nabla b|^{0.33}\ (Rd_{90})^{0.45}} \qquad \text{for} \quad |\nabla b| > 0.6\% \\
\frac{1}{n_r} &= \frac{2.73\, g^{0.49}(H\,|\mathbf{u}|)^{0.03}}{|\nabla b|^{0.08}\ (Rd_{90})^{0.24}}, \qquad \text{for} \quad |\nabla b| \leq 0.6\%,
\end{aligned} \tag{4}$$

where d_{90}, as customary, denotes the value such that 90% of the soil sediment has grain diameter $d \leq d_{90}$. Notice that we have introduced a roughness coefficient R that multiplies d_{90} in the formulation above, to be used to account for model incompleteness and intrinsic model errors. This is the only empirical parameter that is not directly derived from data but left instead to be determined by model calibration experiments, see the discussion in Section 7.2. In order to allow for regions with very small values of the slope, the Manning coefficient actually used in the model is defined as $n = \max\{n_r, n_{min}\}$, where a minimum value n_{min} is set by the user depending on the specific application. For all the simulations performed in this paper, we assume $g = 9.81\ m\ s^{-2}$ and $n_{min} = 0.01\ s\ m^{-\frac{1}{3}}$.

The model is then completed by a number of equations for the time evolution of the equivalent depths of other two-dimensional, vertically averaged water and sediment layers, which are all defined for $\mathbf{x} \in \Omega_b$. More specifically, we consider a snow layer with equivalent depth h_{sn}, a gravitational layer with equivalent depth h_g and a sediment layer with equivalent depth h_{sd}. For each of these layers, conservation of mass is assumed, so as to obtain

$$\begin{aligned}
\partial_t h_{sn} &= \mu p - s, \\
\partial_t h_{sd} + \nabla \cdot \mathbf{f}_{sd}(h_{sd}, \mathbf{u}) &= w \\
\partial_t h_g + \nabla \cdot \mathbf{f}_g(h_g) &= s + f - ev.
\end{aligned} \tag{5}$$

Here $\mathbf{f}_{sd}, \mathbf{f}_g$ denote the sediment and gravitational layer fluxes, while p, s, f denote, as before, the precipitation, snowfall and infiltration rates, respectively, while ev represents the evapotraspiration rate and w is the sediment source rate. For the horizontal mass fluxes and the mass exchanges among layers, relatively simple models are employed in the present formulation, which will now be discussed in greater detail, starting from the topmost layer. Each of these, however, could and should be replaced by more sophisticated approaches, the only limitations being in practice the available data and the computational cost.

The atmosphere is considered as a water reservoir of infinite capacity. Water leaves this reservoir through precipitation, in form of snow or rain, which is characterized by intensity, duration and spatial distribution. On the other hand, water may enter back the atmospheric layer via evapotranspiration. Precipitation can take the form of rain or snow, depending on

the surface temperature. Rain occurs if the temperature is higher than the melting threshold of $T_m = 2\,^{\circ}C$. In this case, water is assumed to end up in the surface run-off layer. In the opposite case, precipitation takes the form of snow and is being accumulated at the surface until temperature reaches values high enough to cause melting. We use a linear relationship between temperature and orography height, based on the International Standard Atmosphere, see e.g. [27]. The snow melting rate s is computed according to the degree-day approach [43], [28]:

$$s = \delta(T - T_m), \tag{6}$$

where δ is a parameter that determines the amount of snow that melts in one day at a given temperature T. The evapotranspiration rate ev is modeled via the Hargreaves equation [40], given by

$$ev = 0.0023\, R_a(T_{mean} + 17.8)\, \sqrt{T_{max} - T_{min}}. \tag{7}$$

Here, R_a is the water equivalent extraterrestrial radiation, T_{mean} is the mean air temperature, T_{max}, T_{min} the daily maximum and minimum air temperatures, measured in Celsius degrees, respectively. The extraterrestrial radiation, R_a, expressed in $[MJ\ m^{-2}\ day^{-1}]$, for each day of the year and for different latitudes can be estimated from the solar constant, the solar declination and the time of the year by:

$$R_a = \frac{24 \cdot 60}{\pi} G_{sc}\, d_r(\omega_s\ \sin\phi\ \sin\delta + \cos\phi\ \cos\delta\ \sin\omega_s), \tag{8}$$

where the solar constant is given by $G_{sc} = 0.0820[MJ\ m^{-2}\ min^{-1}]$, d_r denotes the inverse of the Earth-Sun distance and the sunset hour angle is given by $\omega_s = \arccos(-\tan\phi\ \tan\delta)$, where δ is the solar declination and ϕ is the latitude.

The sediment flux is expressed as a function of the surface run-off velocity and of the local terrain slope. This dependency is modelled following the proposal in [84] as:

$$\mathbf{f}_{sd} = \alpha\ |\nabla b|^{\beta}\ h_{sd}\mathbf{u}, \tag{9}$$

where α and β are empirical coefficients. Possible values for these coefficients are $\alpha = 2.5$ and $\beta = 1.6$, as suggested in [71]. In this model, the critical shear stress is set to zero, so that the sediment movement begins simultaneously with the water movement. The sediment source term w is defined according to the Gavrilović method [8, 34, 35]. It corresponds to the rate of sediment production due to erosive processes as a result of precipitation and it is computed as:

$$w = \pi\,(1 - \mu)\,p\,\tau_g\,Z^{3/2}. \tag{10}$$

Terms τ_g and Z are empirical coefficients that depend on temperature and land use, respectively, while p is the precipitation intensity. Although the

Gavrilović method gives results on a yearly basis, it is assumed that it is also valid for shorter periods in which w will be interpreted as an intensity.

The gravitational layer is the soil portion in which water can move due to gravitational forces. This movement is governed mainly by the permeability of the soil. For the present version of the model, the same, extremely simplified description of the subsurface mass fluxes is adopted as in [8]. More specifically, the horizontal mass fluxes in the gravitational layer $\mathbf{f}_g$ are defined as:

$$\mathbf{f}_g(h_g) = h_g \mathbf{u}_g, \tag{11}$$

where $\mathbf{u}_g$ represents the water velocity vertically averaged over the layer. This velocity is modeled as $\mathbf{u}_g = \beta_g(h_g, \mathbf{x})\mathbf{n}$, where β_g is the hydraulic conductivity, a function of the soil permeability and of the water level in the layer, while $\mathbf{n} = -\nabla b/|\nabla b|$. We estimate the hydraulic conductivity from the characteristic diameters of the soil particles using the Hazen model [41], which yields

$$\beta_g = C_H \frac{g}{\nu} d_{10}^2, \tag{12}$$

where C_H is a non dimensional coefficient with a reference value $6.54 \cdot 10^{-4}$, ν is the water kinematic viscosity ($\nu = 0.89 \cdot 10^{-6} m^2/s$ at $25°C$) and d_{10} denotes the value such that 10% of the soil sediment has grain diameter $d \leq d_{10}$. This very crude model will be replaced in future implementations by a more accurate one based on vertically averaged Darcy equations coupled to the surface layer flow, along the lines proposed in several papers, see e.g. [14, 15, 22, 55].

The water infiltration f from the surface run-off layer to the gravitational layer is described by the well known SCS-CN or curve number method, see e.g. [60]. This approach has been very widely applied in practice, also to areas similar to those that will constitute our main case study. On the other hand, the approach has also been strongly criticized in other studies, see e.g. [54]. In this first application of the proposed model, the more conventional SCS-CN model will be employed, while the suggestions for improvements proposed in [54] and other corrections due to the presence of horizontal water fluxes will be investigated in future works.

In order to get the expression of the infiltration rate, we consider the mass conservation laws for surface and gravitational run-off in absence of boundary fluxes, together with the proportionality hypothesis of SCS-CN method:

$$\begin{aligned} &\partial_t H = p - f \\ &\partial_t h_g = f \\ &\frac{F}{S} = \frac{P - F}{P}, \end{aligned} \tag{13}$$

where S is the maximum soil moisture retention and F and P are the time integrals of f and p, respectively. For the maximum soil moisture retention,

we will use the following expression (in mm):

$$S = 254 \left(\frac{100}{CN} - 1 \right), \tag{14}$$

where CN is the non dimensional parameter usually called the curve number. CN varies from 30 to 100 and depends on soil type, land cover and land use. Large values of such parameter are associated with impermeable surfaces, and subsequently to lower storage capability and higher run-off. The US National Resources Conservation Service provides a table in which each type of land cover and land use is associated to four values of CN, depending on the hydrologic soil group, which in turn defines the actual run-off capability of the soil below. Such soil groups are usually identified by a letter, from A to D, where A identifies the most impermeable soils and D the most permeable ones. For example, paved roads are associated with a CN value of 98 regardless of the soil group, woods in fair conditions and favourable soil are associated with a value of 42 and woods with unfavourable soil 80. More details on the criteria used to determine the CN values will be given in Sections 5 and 7.

Finally, in order to derive an expression for f, we recast the last equation in (13) as:

$$\frac{h_g}{S} = \frac{H}{H + h_g}. \tag{15}$$

It is then possible to solve the system (13) in order to get an expression for F, which denoting with H_0 and $h_{g,0}$ the initial conditions for surface and gravitational run-off, reads:

$$F = \frac{S\,P}{P + S + H_0 + h_{g,0}}, \tag{16}$$

which is the the common expression of the SCS-CN formulation. To get an expression of f, one can derive (15) with respect to time, under the hypothesis of constant S, so as to obtain

$$\partial_t H = \partial_t h_g \left[\frac{S^2}{(S - h_g)^2} - 1 \right]. \tag{17}$$

By substituting (17) in the last equation in (13), one gets for f

$$f = p \left(\frac{S - h_g}{S} \right)^2. \tag{18}$$

Notice that, since $h_g \leq S$, in Equation (18) the precipitation rate is multiplied by a real quantity lying between 0 and 1, which ensures that $f \leq p$. An initial loss, I_a, can be added to this model to represent interception and

depression storage. This loss occurs prior to the onset of run-off. The final infiltration rate model reads then

$$f = \begin{cases} 0, & \text{if } H + h_g < I_a, \\ p \left(\frac{S - h_g}{S} \right)^2, & \text{if } H + h_g > I_a. \end{cases} \tag{19}$$

The initial loss is usually assumed to be proportional to the maximum soil moisture retention $I_a = c\, S$, where c is a real constant usually set equal to values between 0.05 and 0.2.

4 The numerical discretization

The De Saint Venant equations (1) are discretized via the semi-implicit approach first proposed in [13, 17] and subsequently applied to a large number of coastal and river circulation models. In this way the numerical stability of the scheme depends on the velocity based Courant number $\Delta t \left| \mathbf{u} \right| / \Delta x$, rather than on the celerity based Courant number $\Delta t \sqrt{gH} / \Delta x$. The stability condition based on the latter can be much more restrictive if water bodies of significant depth are present in the simulation domain. This allows one to use larger values of the time step compared to those required by classical explicit schemes, see e.g. [49]. An application or the same method to two-dimensional sediment transport in rivers is presented in [68], while a one-dimensional, section averaged model for river hydraulics based on a similar approach is presented in [31, 67]. While higher order variants in space and time of this approach can be devised, in this work we will stick to the simplest, first order formulation, since high order formal accuracy is less relevant than robustness for the target applications.

We consider a Cartesian structured mesh with resolution Δx, Δy on the whole computational domain $\Omega = [0, L_x] \times [0, L_y]$ and a time step Δt. While for simplicity the time step is assumed to be constant in this Section, in practice an option for the adaptive choice of the time step has been implemented, which is especially useful in realistic applications, as it will be shown in Section 7.2. The adaption mechanism chooses time step values up to a prescribed multiple of the Courant number $\Delta t \sqrt{gH} / \Delta x$ for the surface layer. In this way, a smaller time step is automatically chosen in case of intense rainfall events, thus allowing for better time resolution of critical events. A staggered variable arrangement is employed, with discrete velocity variables $u^n_{i+\frac{1}{2},j}$ and $v^n_{i,j+\frac{1}{2}}$ defined at half integer locations and discrete variables $\eta^n_{i,j}, H^n_{i,j}$ defined at integer locations. Wet cells are defined as those for which $H^n_{i,j} > H_d$. These cells provide a discretization of the drainage domain Ω_d. The space and time discretization is given for all wet cells and corresponding edges by:

$$
\begin{aligned}
\eta_{i,j}^{n+1} &= \eta_{i,j}^{n} - \frac{\Delta t}{\Delta x}\left[H_{i+\frac{1}{2},j}^{n} u_{i+\frac{1}{2},j}^{n+1} - H_{i-\frac{1}{2},j}^{n} u_{i-\frac{1}{2},j}^{n+1}\right] \\
&- \frac{\Delta t}{\Delta y}\left[H_{i,j+\frac{1}{2}}^{n} v_{i,j+\frac{1}{2}}^{n+1} - H_{i,j-\frac{1}{2}}^{n} v_{i,j-\frac{1}{2}}^{n+1}\right] \\
&+ \Delta t\,(1-\mu)\,p_{i,j}^{n} - \Delta t\, f_{i,j}^{n}, \qquad (20) \\
u_{i+\frac{1}{2},j}^{n+1} &= \mathcal{F}u_{i+\frac{1}{2},j}^{n} - g\frac{\Delta t}{\Delta x}(\eta_{i+1,j}^{n+1} - \eta_{i,j}^{n+1}) \\
&- \Delta t \gamma_{i+\frac{1}{2},j}^{n} u_{i+\frac{1}{2},j}^{n+1}, \qquad (21) \\
v_{i,j+\frac{1}{2}}^{n+1} &= \mathcal{F}v_{i,j+\frac{1}{2}}^{n} - g\frac{\Delta t}{\Delta y}(\eta_{i,j+1}^{n+1} - \eta_{i,j}^{n+1}), \\
&- \Delta t \gamma_{i,j+\frac{1}{2}}^{n} v_{i,j+\frac{1}{2}}^{n+1}. \qquad (22)
\end{aligned}
$$

Here $\mathcal{F}u_{i+\frac{1}{2},j}^{n}$, $\mathcal{F}v_{i,j+\frac{1}{2}}^{n}$ denote some explicit discretization of the momentum advection terms. In this work, a first order semi-Lagrangian method with bilinear interpolation is employed. Furthermore, the water layer depths $H_{i+\frac{1}{2},j}^{n}$, $H_{i,j+\frac{1}{2}}^{n}$ are defined in an upwind fashion, so that

$$
H_{i+\frac{1}{2},j}^{n} = H_{i+1,j}^{n} \quad \text{if} \quad u_{i+\frac{1}{2},j}^{n+1} < 0
$$

$$
H_{i+\frac{1}{2},j}^{n} = H_{i,j}^{n} \quad \text{if} \quad u_{i+\frac{1}{2},j}^{n+1} > 0,
$$

as suggested in [36]. While the method defined by (20) is only first order in time and space, the resulting discretization is very robust and stable. The practical solution of equations (20) is achieved as follows. The equations for $u_{i+\frac{1}{2},j}^{n+1}$, $v_{i,j+\frac{1}{2}}^{n+1}$ are first rewritten as

$$
\begin{aligned}
u_{i+\frac{1}{2},j}^{n+1} &= \alpha_{i+\frac{1}{2},j}^{n}\mathcal{F}u_{i+\frac{1}{2},j}^{n} - g\alpha_{i+\frac{1}{2},j}^{n}\frac{\Delta t}{\Delta x}(\eta_{i+1,j}^{n+1} - \eta_{i,j}^{n+1}) \qquad (23) \\
v_{i,j+\frac{1}{2}}^{n+1} &= \alpha_{i,j+\frac{1}{2}}^{n}\mathcal{F}v_{i,j+\frac{1}{2}}^{n} - g\alpha_{i,j+\frac{1}{2}}^{n}\frac{\Delta t}{\Delta y}(\eta_{i,j+1}^{n+1} - \eta_{i,j}^{n+1}) \qquad (24)
\end{aligned}
$$

where

$$
\alpha_{i+\frac{1}{2},j}^{n} = \frac{1}{1+\Delta t\gamma_{i+\frac{1}{2},j}^{n}}, \quad \alpha_{i,j+\frac{1}{2}}^{n} = \frac{1}{1+\Delta t\gamma_{i,j+\frac{1}{2}}^{n}},
$$

respectively. These equation are then substituted into the equation for $\eta_{i,j}^{n+1}$, so as to obtain, for the interior nodes, the equations

$$
\begin{aligned}
\eta_{i,j}^{n+1} = \mathcal{G}_{i,j}^{n} \quad &- \quad g\frac{\Delta t^2}{\Delta x^2}\alpha_{i+\frac{1}{2},j}^{n} H_{i+\frac{1}{2},j}^{n}(\eta_{i+1,j}^{n+1} - \eta_{i,j}^{n+1}) \\
&+ \quad g\frac{\Delta t^2}{\Delta x^2}\alpha_{i+\frac{1}{2},j}^{n} H_{i-\frac{1}{2},j}^{n}(\eta_{i,j}^{n+1} - \eta_{i-1,j}^{n+1}) \\
&- \quad g\frac{\Delta t^2}{\Delta y^2}\alpha_{i,j+\frac{1}{2}}^{n} H_{i,j+\frac{1}{2}}^{n}(\eta_{i,j+1}^{n+1} - \eta_{i,j}^{n+1}) \\
&+ \quad g\frac{\Delta t^2}{\Delta y^2}\alpha_{i,j-\frac{1}{2}}^{n} H_{i,j-\frac{1}{2}}^{n}(\eta_{i,j}^{n+1} - \eta_{i,j-1}^{n+1})
\end{aligned}
$$

where

$$
\begin{aligned}
\mathcal{G}_{i,j}^{n} \quad &= \quad \eta_{i,j}^{n} + \Delta t(1-\mu)p_{i,j}^{n} - \Delta t f_{i,j}^{n} \\
&- \quad \frac{\Delta t}{\Delta x}\left[H_{i+\frac{1}{2},j}^{n}\alpha_{i+\frac{1}{2},j}^{n}\mathcal{F}u_{i+\frac{1}{2},j}^{n} - H_{i-\frac{1}{2},j}^{n}\alpha_{i-\frac{1}{2},j}^{n}\mathcal{F}u_{i-\frac{1}{2},j}^{n}\right] \\
&- \quad \frac{\Delta t}{\Delta y}\left[H_{i,j+\frac{1}{2}}^{n}\alpha_{i,j+\frac{1}{2}}^{n}\mathcal{F}v_{i,j+\frac{1}{2}}^{n} - H_{i,j-\frac{1}{2}}^{n}\alpha_{i,j-\frac{1}{2}}^{n}\mathcal{F}v_{i,j-\frac{1}{2}}^{n}\right].
\end{aligned} \tag{25}
$$

Equation (25) can be rewritten as

$$
\begin{aligned}
&\left[1 + g\frac{\Delta t^2}{\Delta x^2}\left(\alpha_{i+\frac{1}{2},j}^{n}H_{i+\frac{1}{2},j}^{n} + \alpha_{i-\frac{1}{2},j}^{n}H_{i-\frac{1}{2},j}^{n}\right)\right. \\
&\left. \quad + g\frac{\Delta t^2}{\Delta y^2}\left(\alpha_{i,j+\frac{1}{2}}^{n}H_{i,j+\frac{1}{2}}^{n} + \alpha_{i,j-\frac{1}{2}}^{n}H_{i,j-\frac{1}{2}}^{n}\right)\right]\eta_{i,j}^{n+1} \\
&- g\frac{\Delta t^2}{\Delta x^2}\alpha_{i+\frac{1}{2},j}^{n}H_{i+\frac{1}{2},j}^{n}\eta_{i+1,j}^{n+1} - g\frac{\Delta t^2}{\Delta x^2}\alpha_{i-\frac{1}{2},j}^{n}H_{i-\frac{1}{2},j}^{n}\eta_{i-1,j}^{n+1} \\
&- g\frac{\Delta t^2}{\Delta y^2}\alpha_{i,j+\frac{1}{2}}^{n}H_{i,j+\frac{1}{2}}^{n}\eta_{i,j+1}^{n+1} - g\frac{\Delta t^2}{\Delta y^2}\alpha_{i,j-\frac{1}{2}}^{n}H_{i,j-\frac{1}{2}}^{n}\eta_{i,j-1}^{n+1} = \mathcal{G}_{i,j}^{n}.
\end{aligned} \tag{26}
$$

These equations, defined for all wet cells, define a linear system whose matrix is symmetric, positive definite and diagonally dominant, thus guaranteeing the possibility of a fast and accurate numerical solution via efficient numerical linear algebra solvers. In particular, we have used the conjugate gradient method with an incomplete Cholesky factorization preconditioner, see e.g. [46], as implemented in the Eigen library [39], with a tolerance equal to 10^{-6}.

Notice that, since the velocities are taken to be zero at the interfaces between wet and dry cells, the boundary conditions for system (25) are equivalent to discrete homogeneous Neumann conditions for the free surface $\eta_{i,j}^{n+1}$. If instead a cell has an edge that belongs to $\partial\Omega_d \cap \partial\Omega_b$, imposing outflow boundary conditions also results in assuming the same kind of boundary conditions. All other equations in (5) are discretized by a finite volume approach over each cell of the computational domain, with first order upwind

definitions of the numerical fluxes $f_{i\pm\frac{1}{2},j}, f_{i,j\pm\frac{1}{2}}$ and explicit Euler time discretization, see e.g. [49]. Notice that, since Courant number larger than one are allowed for the surface water layer dynamics, the discretization of the sediment transport equation in (5) is performed with a time step that is a fraction of that used for the surface layer itself.

As remarked above, the previously outlined approach has good robustness and stability properties. However, when applied on mountainous terrain, very large and unphysical velocity values can still arise in presence of very large values of the orographic slope, especially during intense rainfall events. It is to be remarked that, in these regions, the hydrostatic approximation that is at the basis of the model equations breaks down, so that one cannot expect these equations to provide an accurate description of the flow. In order to avoid that the model accuracy is affected by these spurious velocities, we have therefore also implemented a model option that excludes from the computational domain cells with a slope value above a given user defined slope threshold. These large slope regions are treated as reservoirs of water and sediment for the rest of the computational domain. Mass conservation is still guaranteed when using this option, since the integrated precipitation and sediment source terms corresponding to the large slope regions provide to the water and sediment fluxes into the lowest altitude cell neighbouring each of these regions. It will be shown in Section 7.2 that this option allows to improve the quality of the results, as well as improving the efficiency if the time step adaptation mechanism is not employed.

5 Data preprocessing

For practical applications of the model described in the previous sections, several input datasets must be made available, including in particular orography data and soil composition data. The former is usually provided by easily accessible Digital Terrain Models (DTM). The depression filling algorithm described in [6] and also used in [7] has been implemented as part of the model preprocessing package. In this approach, all DTM depressions or pits are filled to the level of their lowest outlet or spill-point. As it will be shown, however, the numerical discretization implemented in the model is such that this form of preprocessing is not necessary for the model to produce accurate results.

The preprocessing of soil composition data requires instead a special treatment, since the relevant data are rarely available at the scales of interest for the application of the proposed model. For this reason, a geostatistical preprocessor has been developed, described in greater detail in [32], which downscales to fine resolution meshes the soil composition data available in global databases such as SoilGrids [42] and blends it with data from field measurements. The key concepts underlying this preprocessor will be briefly

reviewed here.

The potential maximum soil moisture retention is a function of soil texture, which can in turn be determined from particle-size fractions, i.e. the relative percentages of clay, silt and sand in the soil, see e.g. [52]. These are compositional data (CoDa), as the sum particle-size fractions have non negative values and their sum is always equal to one. For this type of data, well established statistical approaches have been developed in the literature of Compositional Data Analysis [58], to deal with the data constraints and to avoid spurious correlations among the recovered ratios [4, 48]. Consistent with this literature stream, in our approach, the particle-size fractions are transformed via an Isometric Log Ratio transform [51], so as to be able to work within the Aitchison geometry for CoDa without modifying the classical statistical techniques based on the Euclidean metric. Data coming from larger scale databases are then downscaled to match the desired resolution using the Isometric Log-Ratio Area-To-Point Regression Co-Kriging (ILR-ATPRCoK) as described in [32]. Notice that the same approach also allows one to perform a geostatistical Conditional Simulation, [72], in order to analyze, in a Monte Carlo setting, how the uncertainty propagates to the output of a numerical simulation. A first application of this model capability is presented in Section 7.4, while its more systematic deployment will be the focus of future developments of our approach.

Since the data obtained from global databases such as SoilGrids are only available at a very low resolution, large discrepancies can be found between these downscaled particle-size fractions and those obtained from field measurements. To face this issues, the statistical preprocessor described in [32] was modified to allow for the consideration of field data which are deemed more representative of the granulometric distribution of some areas of the domain (e.g. river beds). This is here done by dividing the computational domain into two subdomains. In the first one, the estimation of particle-size fractions is mostly driven by the global database, while in the other subdomain it is mostly influenced by the field data. These subdomains are separated by a transitional area where the results of the two estimation procedures are blended to obtain a reasonably smooth transition. This technique will be described in greater detail in Section 7.

6 Simulations with idealized orography

In a first attempt at verification of the model implementation, we have performed several simulations with idealized orography profiles where, for simplicity, the computational domain coincides with the basin and $\Delta x = \Delta y = \Delta$. In these tests, we consider null initial conditions, we keep the time step constant and we do not exclude higher slope regions from the computational domain. In a first simulation, we consider a domain with

$L_x = 10\ km, L_y = 10\ km$ with non-reflecting boundary conditions at the boundary of the basin domain. The orographic profile is given by

$$b(x,y) = 15 - 80\frac{(x - L_x/2)^2 + (y - L_y)^2}{L_x^2} + 300\frac{(x - L_x/2)^4 + (y - L_y)^4}{L_x^4} + 2 + 0.0005\, L_y + 0.0005x - 0.0005y,$$

whose isolines are plotted in Figure 1a. It can be seen that four depressions are present over the domain. We consider an impermeable and non erodible soil, so that only the discretization of the surface water layer is being tested and no preprocessing of the orography is applied. A period of 5 days is simulated, over which a constant and uniform rainfall intensity of $1\ mm\, h^{-1}$ on the whole basin domain is considered. A computational mesh with $\Delta = 100\ m$, is considered and the time step was taken to be $\Delta t = 36\ s$, which corresponds to approximately 100 time steps per hour. The isolines of the surface run-off layer at the final time are plotted in Figure 1b, highlighting the formation of four lakes at the bottom of the orographic depressions. The absolute value and direction of the velocity field at the final time are plotted in Figure 1c,d. It is to be remarked that the Courant number based on the celerity $\sqrt{gH}$, computed considering the deepest portion of the small lakes, is approximately 3, which highlights the method's capability to employ a time step much longer than that required by classical explicit time discretizations, which are of almost universal use in the models reviewed in Section 2.

In a second set of simulations, in which also infiltration and motion of the gravitational layer are considered, the domain is a square with $L_x = 10\ km, L_y = 10\ km$ with an orographic profile given by the plane

$$b(x,y) = 2 + 0.0005\, L_y + 0.0005x - 0.0005y.$$

A computational mesh with $\Delta = 100\ m$ and a time step $\Delta t = 72\ s$ are considered, which corresponds to 50 time steps per hour. The soil properties are defined here by a constant curve number $CN = 79$. In a first simulation, we consider a period of 20 days, over which a constant and uniform rainfall of $5\ mm\ h^{-1}$ is assumed. We apply reflecting boundary conditions on the water height H at the boundary of the basin domain. In Figure 2a we plot the time evolution of the gravitational layer water content averaged over the whole domain. It can be observed that, as the soil reaches the saturated conditions corresponding to the maximum soil moisture retention, the infiltration rate approaches zero, see Figure 2b. Finally, in Figure 2c,d the spatial distribution of the state variables associated to the surface water layer is plotted at the final time. It can be observed that the lower portion of the domain is correctly being filled by the surface water layer.

We have then performed a multi-event simulation on the same basin, in order to test the model response to time dependent rainfall rates. In this case, we apply non-reflecting boundary conditions on the water height H at

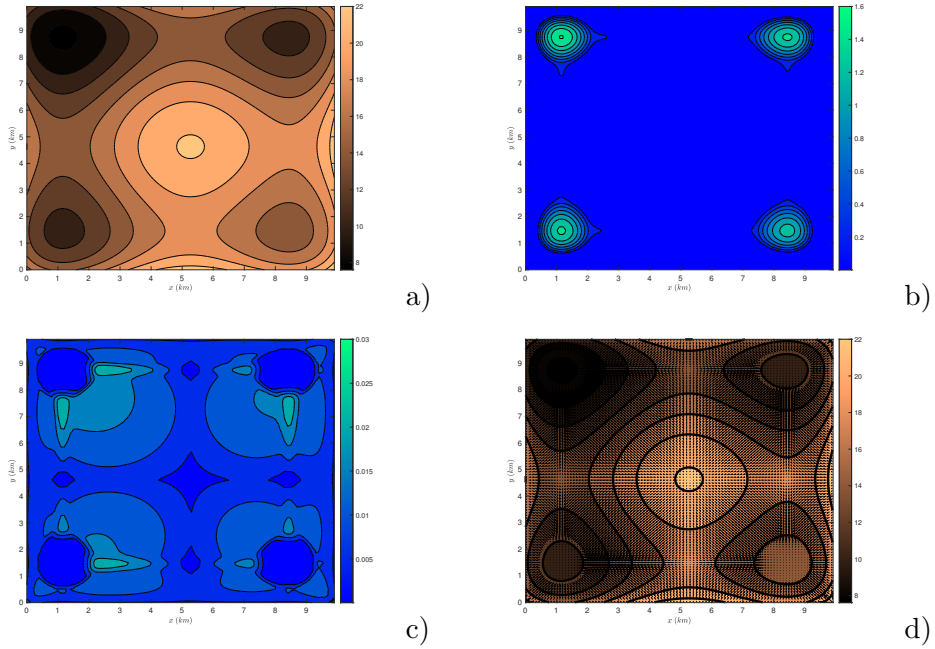

Figure 1: First idealized test: a) orography profile b) final surface layer thickness c) absolute value of velocity field d) direction of velocity field.

the boundary of the basin domain and we also consider evapotranspiration and soil erodibility. We apply a homogeneous rainfall rate of $5\,mm\,h^{-1}$ over the whole basin for a sequence of 5 days long intervals, followed by intervals without precipitation so that the days with precipitation amount to 20% of the total of 365 simulated days. Figure 3b shows the temperature profile input of the simulation, which is necessary in this case to feed the evapotranspiration and the Gavrilović source term of the solid transport equation. The temperature behaviour reflects a typical time series at midlatitudes for a time span of one year starting just after the summer. Figure 3c,d show the time evolution of the average water content in the gravitational layer, maximum soil moisture retention and infiltration rate. It can be seen that the complementary behaviour of the average water content in the gravitational layer and infiltration rate already shown in the previous test is reproduced also with time dependent precipitation forcing.

7 Simulations with realistic orography

In this section, the results of more realistic simulations are reported, including some first comparison with field data available for a specific catchment. As it will be seen, the model is still far from full quantitative agreement with the available data and a number of further improvements and calibration

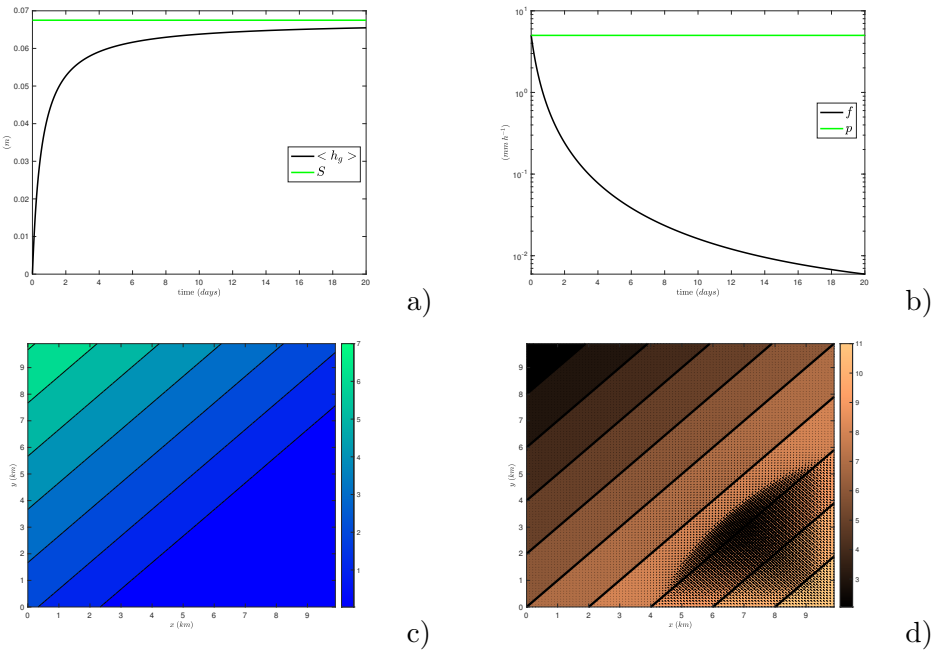

Figure 2: Second idealized test, single event simulation: a) time evolution of average water content in the gravitational layer (black) and maximum soil moisture retention (green) b) time evolution of mean infiltration rate (black) and precipitation rate (green) c) isolines at final time of water content in the surface layer in m d) surface water velocity field at final time, superimposed onto the orography isolines.

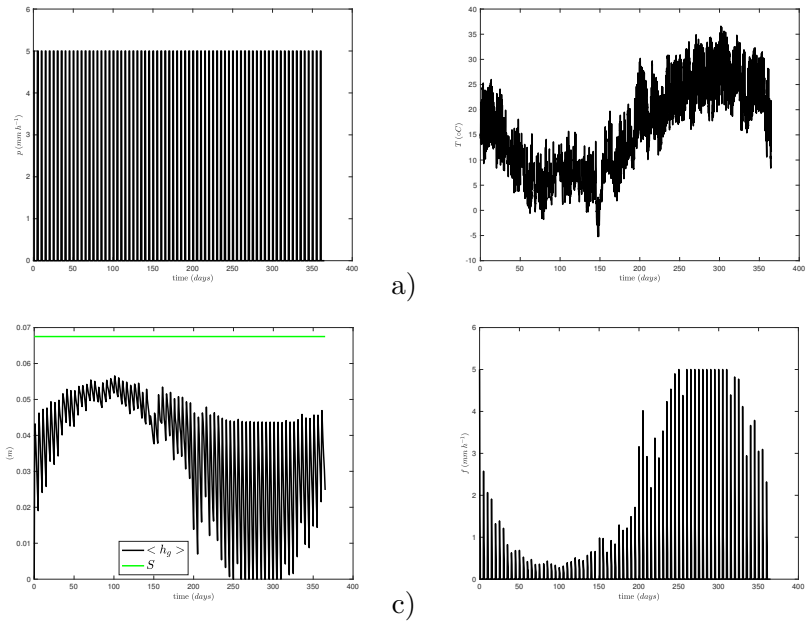

Figure 3: Second idealized test, multi event simulation: time evolution of a) precipitation rate b) temperature c) average water content in the gravitational layer (black) and maximum soil moisture retention (green); d) infiltration rate.

experiments are necessary to turn it into a fully reliable operational tool. However, the results obtained show that it is able to reproduce correctly the main hydrographic features of the considered catchment, to achieve a good estimate of the order of magnitude of the total sediment yield and to perform uncertainty quantification experiments at a limited computational cost.

7.1 Data preprocessing and simulation setup

In a set of simulations with more realistic orography, we have considered a domain corresponding to the Caldone catchment, which is located in the vicinity of the city of Lecco (Northern Italy) and crossed by the small river with the same name. The hydrographic catchment covers an area of $28\,km^2$. The land cover of the catchments mainly includes forests (67%), herbaceous vegetation (16%) and urban areas (13%), according to the CORINE Land Cover Classification (CLC) [10, 11]. For more details on the river catchment structure, we refer to [44]. As in most pre-Alpine environments, active geomorphic processes include colluvial and fluvial transport responsible for the yield and propagation of sediment downstream. In Figures 4 a), b), we represent the DTM and the CLC map for the case study at a resolution of $\Delta = 5\,m$, respectively. In Figure 4 a) we also report the location of two control points where sediment collection tanks are located (blue dots) and that of the control point where the surface water height and discharge are monitored (red dot). In Figure 4 c) we show the slope field (in degrees), while 4 d) displays the same field after removal of the regions with slope values larger than 100% (highlighted in grey).

The data preprocessor presented in section 5 has been applied at a resolution of $\Delta = 5\,m$ to produce the soil compositional data (particle size fractions, denoted in the following as psf) employed in the simulation. In particular, the ILR-ATPRCoK approach was applied combining both SoilGrids data and the field data described in [59, 76]. Since the field data were collected almost exclusively at the bottom of valleys, the catchment was subdivided into three subdomains, based on the local value of the orography slope. Below the threshold value of $s_{inf} = 20$ degrees, only the field data were used as input for the preprocessor, while above the value $s_{sup} = 30$ degrees, only SoilGrids data were used. For cells with slopes in the interval $[s_{inf}, s_{sup}]$, the weighted average

$$\chi = \frac{(s_{sup} - s)\chi_f + (s - s_{inf})\chi_g}{s_{sup} - s_{inf}} \tag{27}$$

was used to compute the compositional value χ. Here, χ_f denotes the compositional value obtained from the field data only and χ_g the one obtained from global SoilGrids data only, respectively. After determining the compositional data, for each cell granulometric curves were obtained from the data

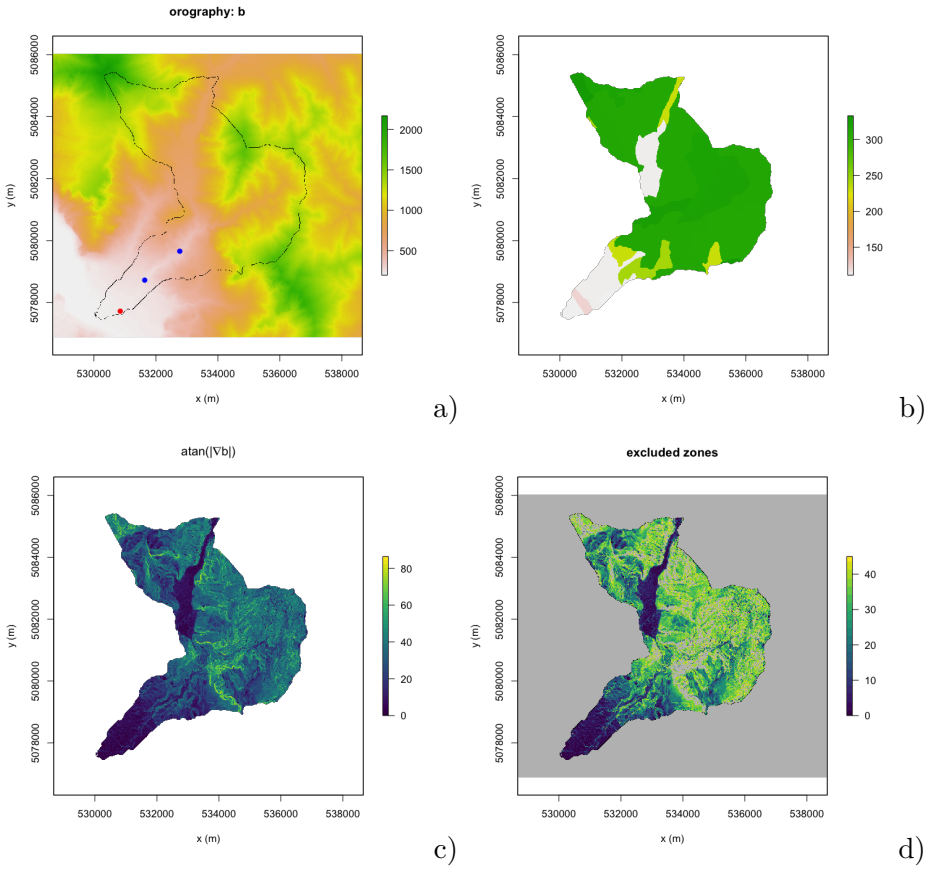

Figure 4: a) 5 m-resolution DTM of the study area, in black we represent the polygon identifying the boundary of the Caldone basin where the non-reflecting boundary conditions are applied, blue points identify the mean location of the tanks considered for the sediment transport and the red point is the control point for the superficial water height b) CLC map c) slope of 5 m-resolution DTM d) slope of 5 m-resolution DTM after removal of areas with more than 100% slope.

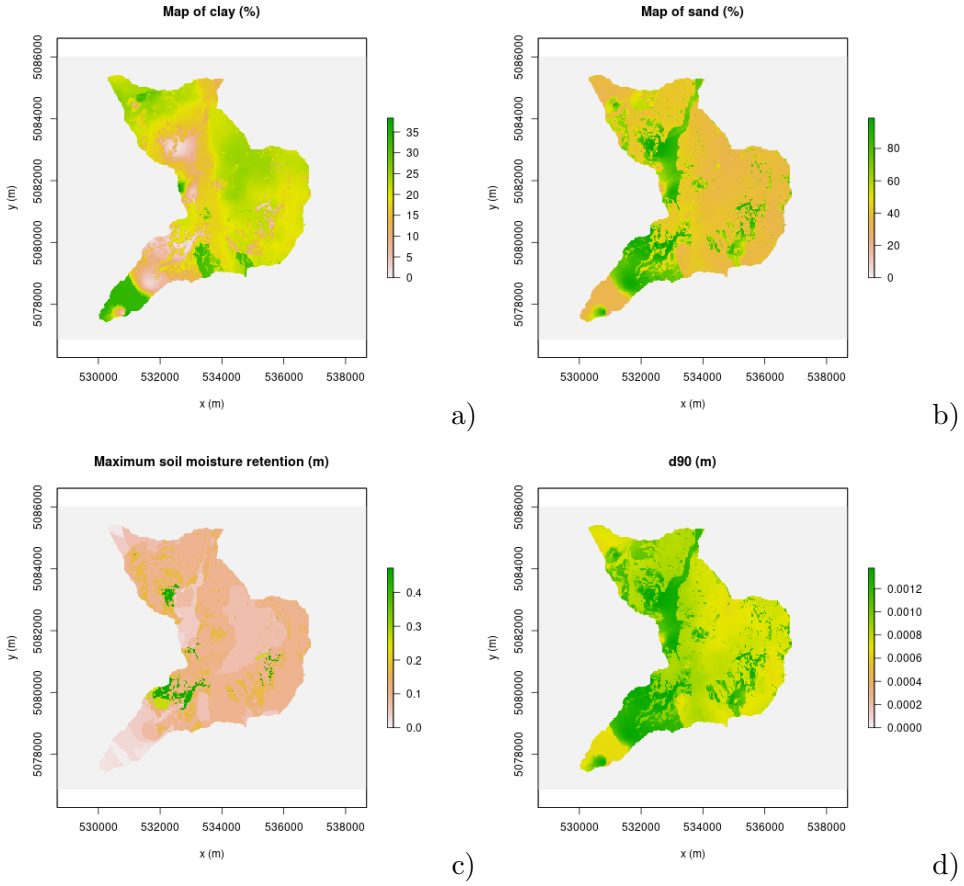

Figure 5: Maps of soil data obtained with blended ILR-ATPRCoK procedure: a) clay psf b) sand psf c) maximum soil moisture retention S d) d_{90}.

by linear interpolation and the d_{10}, d_{90} parameter values were determined from these curves for each cell. An example of the sand and clay compositions, maximum soil moisture retention S and d_{90} in the final compound dataset is shown in Fig. 5.

In all simulations, the precipitation term p is taken to be a space-time dependent field. Data coming from nine rain gauges at different locations in the catchment were used, available from the regional hydrological service [50]. A two dimensional map was derived via the Inverse Distance Weighting (IDW) method, see e.g. [19]. Since data on soil moisture content are not readily available, for all simulations the following initialization procedure was followed. Firstly, the model was run starting from a dry gravitational layer, assuming a constant precipitation rate of 20 mm/h for a preliminary period of 4 days, followed by another 4 days without precipitation. The output of this run was then used to initialize the actual simulation.

Two main kinds of data were employed for the sensitivity analysis and the model calibration. Firstly, water depth and discharge values recorded at the monitoring station denoted by the red dot in Figure 4a) were used for a comparison with the model results. This monitoring station is located on the Caldone river bed. Since the model resolution is coarser than what would be necessary to resolve accurately the river bed, the simulated river bed does not exactly correspond to the real one. For this reason, the comparison with these data was done considering the model output in all the cells nearest to the location of the monitoring station. As a consequence, for each model resolution multiple outputs will be compared to the measured data. Furthermore, data concerning two sediment accumulation tanks located at the blue dots in Figure 4a) were also used. In particular, the data measured at the location closest to the water depth and discharge monitoring station were considered. In this case, the total cumulated sediment inflow corresponding to the cells nearest to the tank was summed to provide results for comparison with the available data.

7.2 Sensitivity to roughness coefficient values and inclusion of large slope regions

In a first attempt to assess the sensitivity of the model to the choice of the empirical roughness parameter R, we have run simulations of an intense rain period consisting of the 35 days comprised between October 26 and November 30 2018, at resolutions $\Delta = 50\,m$ and $\Delta = 35\,m$, respectively. Different values of R were employed, as shown in Figures 6, 7. Notice that, as explained above, the model output at different locations around the monitoring stations is reported. It can be observed that the data falls in the envelope of the model curves, with peak value correctly simulated only for one of the model cells. On the other hand, too high water levels are observed for a long period after each peak at all locations. This unphysical effect still requires deeper investigation and its removal will be addressed in future model versions.

Based on this sensitivity analysis, the value $R = 10^2$ was considered to yield an acceptable compromise between computed peak values for water depth and discharge and intensity of the post-peak spurious effect. For this reason, the value $R = 10^2$ was chosen for the simulations in the rest of the paper. For clarity, only the results computed with this value for the simulation at $\Delta = 35\,m$ resolution are reported in Figure 8. The impact of the exclusion of the large slope regions was also assessed. Results of the simulations in which regions with slope above 100% were excluded (labelled *LS*) are in general not too different from those in which these region were part of the computational domain (labelled *no LS*). However, it can be seen in Figure 9 that the inclusion of the high slope regions results in unrealistic tails in the time series of the water height at the monitoring location.

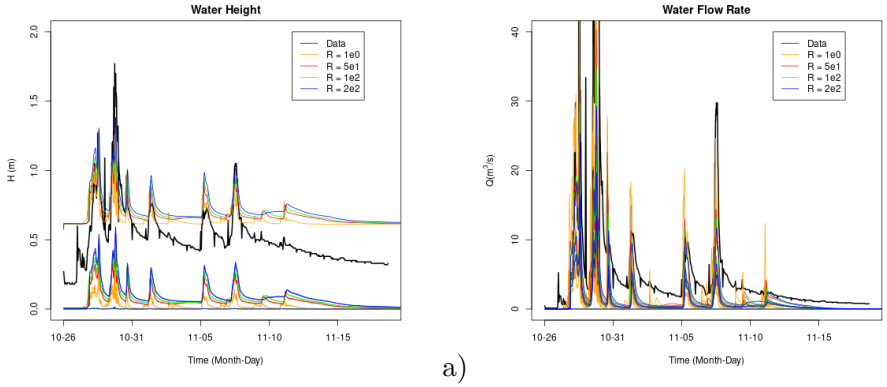

a) b)

Figure 6: Sensitivity analysis with respect to the roughness coefficient values: simulation at $\Delta = 50m$ resolution a) water height b) discharge at monitoring location.

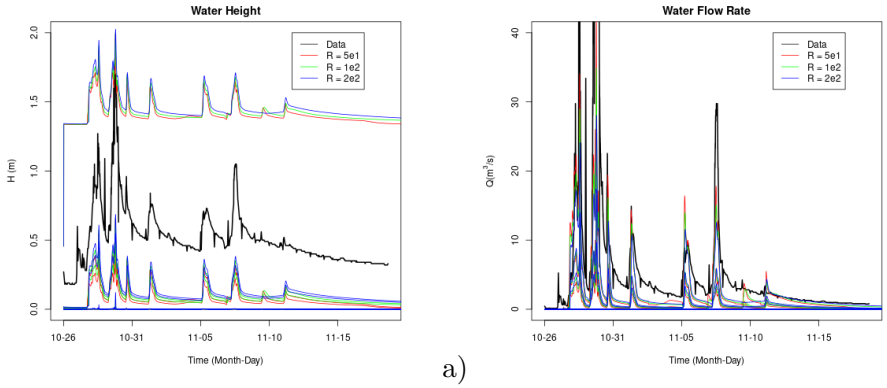

a) b)

Figure 7: Sensitivity analysis with respect to the roughness coefficient values: simulation at $\Delta = 35m$ resolution a) water height b) discharge at monitoring location.

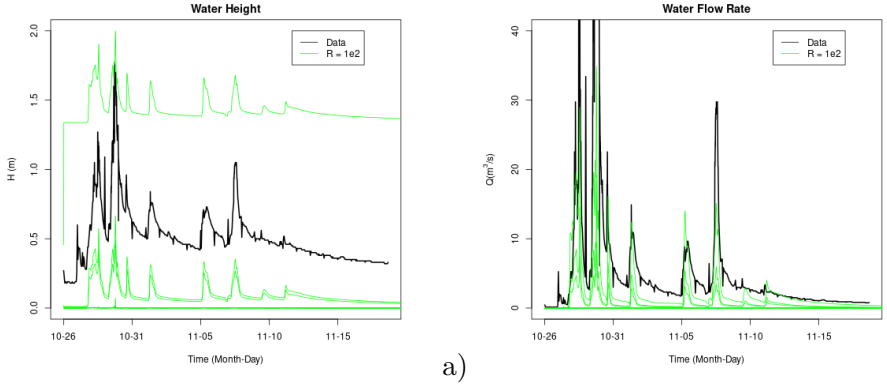

a) b)

Figure 8: Simulation at $\Delta = 35\,m$ resolution with $R = 10^2$, a) water height b) discharge at monitoring location.

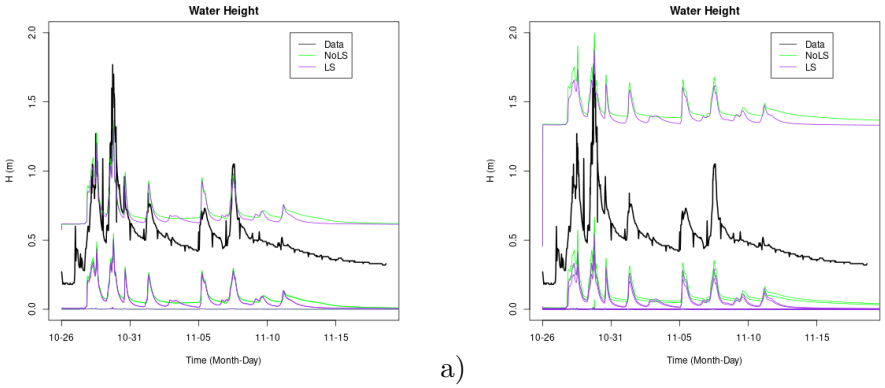

Figure 9: Sensitivity analysis with respect to the inclusion of large slope regions: water height in a) simulation at $\Delta = 50\,m$ resolution b) simulation at $\Delta = 35\,m$ resolution.

These simulations were also used to assess the efficiency of our model implementation. The code was executed on a HPC server node with a Xeon E5-2640 v4 2.4GHz processor. The 35 days simulations at $\Delta = 50m$ required about one hour of CPU time, while the simulations at $\Delta = 35\,m$ required about 4 hours. It has been observed that the time step adaptation mechanism is especially useful in reducing the total computational cost. More specifically, the simulations with adaptive choice of the time step required between 25% and 30% of the CPU time of the corresponding simulations run with fixed time step (choosing the largest value for which the simulation could be completed successfully). The effectiveness of the adaptive choice of the time step can also be seen in Figure 10, where the number of steps required per hour in each of the two simulations is displayed. It can be observed that the time step adaptation mechanism only requires to use very small time steps for relatively short periods that coincide with the peak rainfall events, while much longer time steps can be used most of the time.

7.3 Deterministic one year simulations

Long term deterministic simulations covering the period between September 2017 and September 2018 have also been run at resolutions $\Delta = 50\,m, 35\,m$, and $\Delta = 20\,m$, respectively. On the basis of the discussion in Section 7.2, the simulations were carried out excluding the regions with slope values above 100% and using values of the d_{90} parameter rescaled by the empirical roughness factor $R = 10^2$. In this case, the simulations were run on an Intel i5 2.67GHz processor with 8GB RAM, requiring 7.25, 36.27 and 102.77 hours for the $\Delta = 50\,m, 35\,m$, and $\Delta = 20\,m$, respectively.

An example of the model capability to reproduce realistic run-off patterns without need to prescribe run-off regions *a priori* is shown in Figure

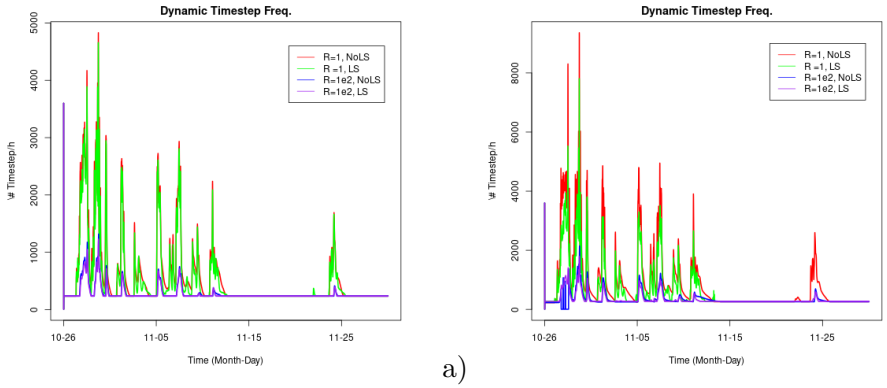

a) b)

Figure 10: Number of time steps used per hour in a) simulations at $\Delta = 50m$ b) simulations at $\Delta = 35\,m$.

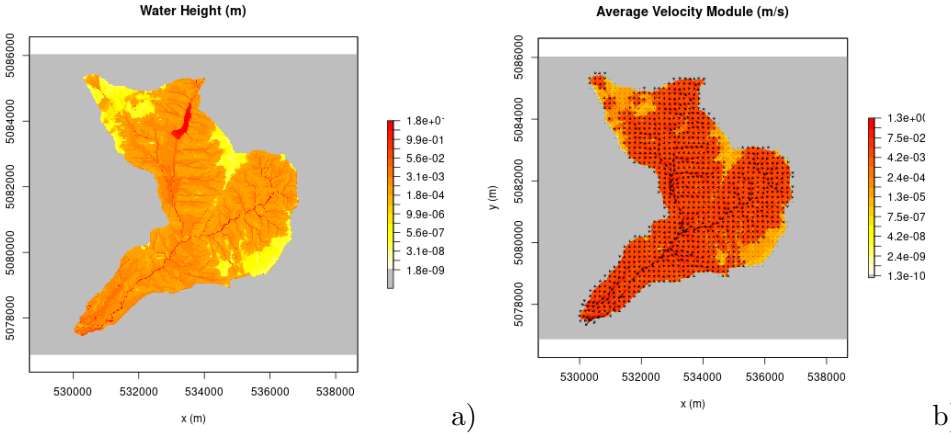

a) b)

Figure 11: Year long simulation at $\Delta = 20\,m$ a) water height b) velocity field at day 181.

11, where the water height and the velocity in the surface layer are displayed at day 181 of the simulation with $\Delta = 20\,m$. It can be noticed that a small lake is formed in a region where small water bodies are indeed present most of the year. The surface water height and the height of the eroded sediment layer at the final time are displayed instead in Figure 12. These results support the main choices made in the model formulation, since reproduction of such fine scale and transient features is unfeasible unless the De Saint Venant equations are solved over the whole computational domain, without *a priori* identification of river beds and other specific run-off regions.

In order to perform a comparison with the available data, the time series of water height and discharge in the same simulation are displayed in Figures 13, 14, 15 for the three different spatial resolutions. As already seen in the preliminary simulation discussed in Section 7.2, it can be observed that the

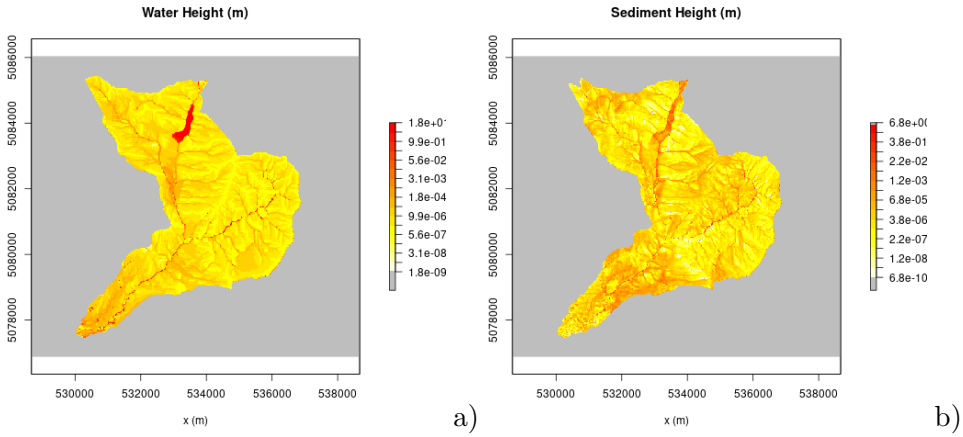

Figure 12: Year long simulation at $\Delta = 20$ a) water height b) sediment layer height at final time.

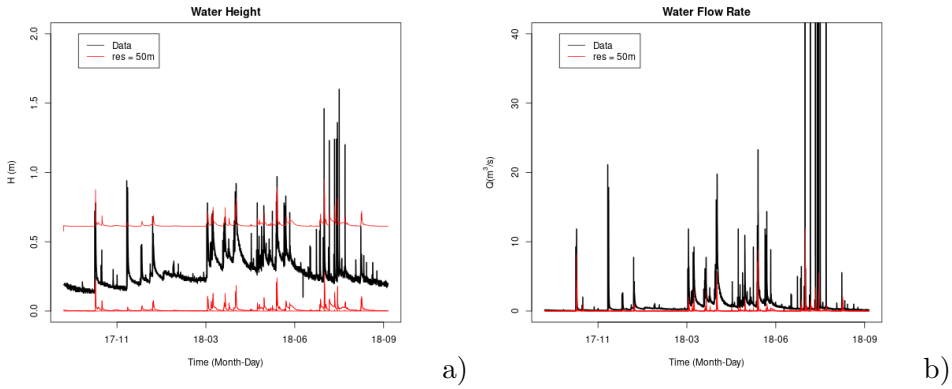

Figure 13: Year long simulations at $\Delta = 50\,m$ resolution: time series of a) water height b) discharge compared with data at monitoring location.

water depth data falls in the envelope of the model curves, with peak value correctly simulated only for a few of the model cells. Again, while the timing of the peak events is captured correctly at all resolutions and the results are qualitatively correct, all simulations also fail to capture correctly the largest discharge peaks. Improving this prediction would probably require further tuning of the empirical roughness coefficient, possibly also in a localized fashion depending on the soil characteristics, as well as an improvement of the friction coefficient models employed.

Furthermore, in Figure 16 we report the time series of the cumulated sediment yield at the monitoring location discussed at the beginning of this Section. The data are normalized with the tank volume, so as to express the fraction of the tank filled by the eroded sediment at each time. It can be observed that, increasing the resolution, the total sediment yield also

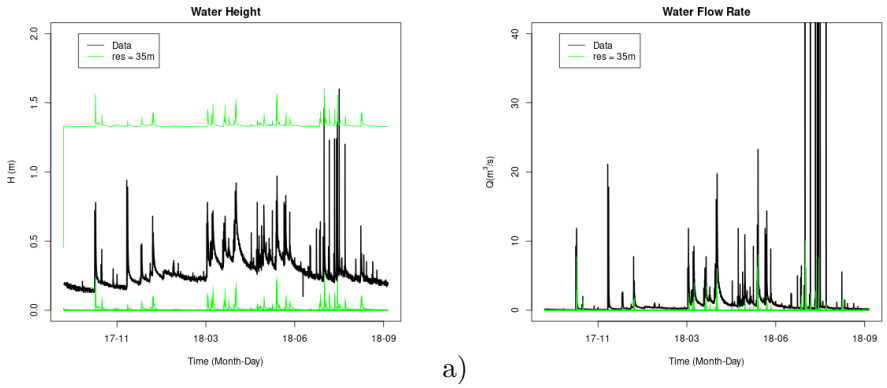

a) b)

Figure 14: Year long simulations at $\Delta = 35\,m$ resolution: time series of a) water height b) discharge compared with data at monitoring location.

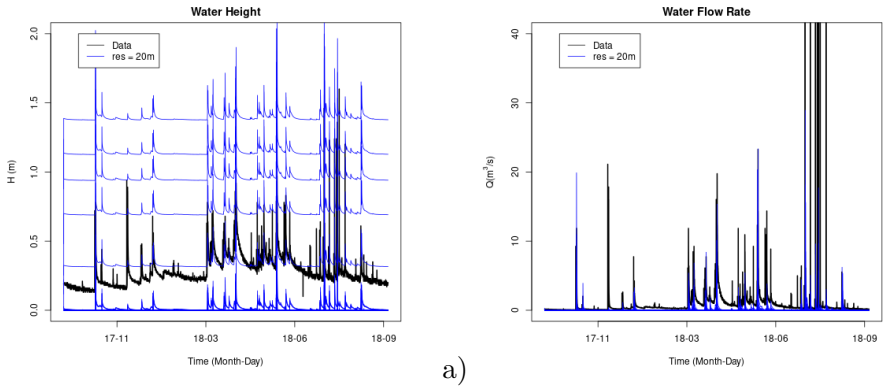

a) b)

Figure 15: Year long simulations at $\Delta = 20\,m$ resolution: time series of a) water height b) discharge compared with data at monitoring location.

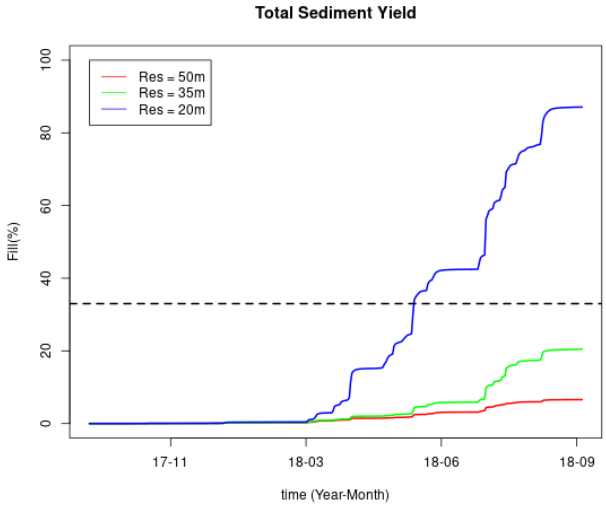

Figure 16: Time series of cumulated sediment yield at monitoring location (percentage of tank filling) in simulations at $\Delta = 50\,m, 35\,m$ and $\Delta = 20\,m$. The horizontal dotted line represents the percentage of tank filling over one year resulting from the measurements described in [45].

increases significantly, achieving a value of approximately 80% filling of the measurement tank at the monitoring location. This is to be compared with the data available in [45], which show an average 33% filling of the measurement tank per year. Even though the orders of magnitude obtained for the eroded volumes correspond to the measured ones, the lack of convergence as resolution increases highlights the need to revise and improve the modelling of the production term (10).

7.4 Monte Carlo simulation of an intense rain period

In order to demonstrate the developed model capabilities for uncertainty quantification and probabilistic forecasting, we have also performed Monte Carlo simulations at resolutions $\Delta = 50\,m$ and $\Delta = 35\,m$, respectively, for the same intense rain period discussed in Section 7.2. The model was initialized with different realizations of the soil compositional data obtained from the geostatistical preprocessor. A total of 50 realizations were performed for each resolution. As in the previous Sections, the simulations were carried out excluding the regions with slope values above 100% and using values of the d_{90} parameter rescaled by the empirical roughness factor $R = 10^2$. For conciseness, we only show and discuss the results of the $\Delta = 35\,m$ simulation. In Figure 17, the time series of water depth and discharge are reported, displaying both the ensemble average and the associated uncer-

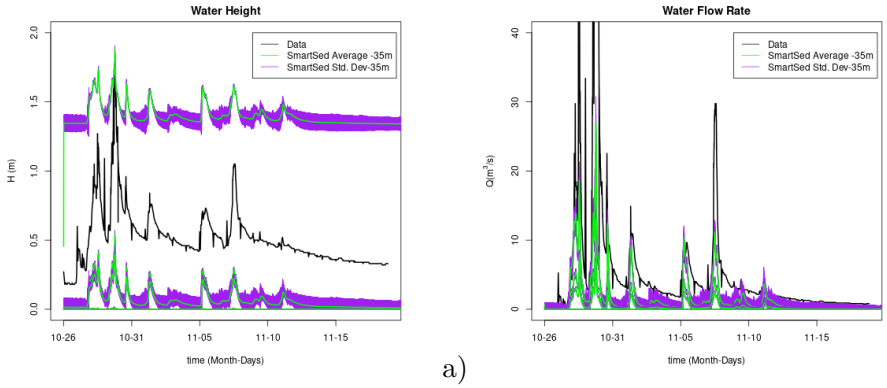

a) b)

Figure 17: Monte Carlo simulations of intense rain period at $\Delta = 35\ m$ resolution: time series of a) water height b) discharge at the monitoring site location. Green line: average over ensemble, purple shading: standard deviation of the ensemble.

tainty, measured by the ensemble standard deviation. The results confirm that substantial bias is still present in the model prediction, which should be addressed by appropriate model improvements as discussed in Section 8. In Figure 18, the distribution of the time series of cumulated sediment yield at monitoring location is shown. Specifically, Figure 18 reports the functional boxplot [75] derived from the 50 realizations of the cumulated sediment yields (as obtained using the R package ROAHD [74]). The probabilistic forecast allows one to identify the central functional quartiles of the simulated distribution and to achieve a robust estimate of a phenomenon well known for the strong associated uncertainties. It can be observed that a rather skewed distribution is obtained, which stresses the need for non trivial statistical methodologies in the uncertainty quantification procedure for these kinds of phenomena.

8 Conclusions

We have presented a numerical model for soil erosion at the basin scale, in which the De Saint-Venantequations are used to model surface water flow over the whole domain, without *a priori* identification of drainage zones. This allows us to model basins in which strong variations of the surface run-off occur without *ad hoc* hypotheses, as well as to include naturally lakes and other water reservoirs. The model is equipped with a geostatistical preprocessor, that downscales to fine resolution meshes the soil composition data available in global databases and integrates them with the available field measurements. The model equations are approximated numerically using a very well tested, efficient and robust semi-implicit discretization method [13, 17]. The proposed technique is able to handle automatically

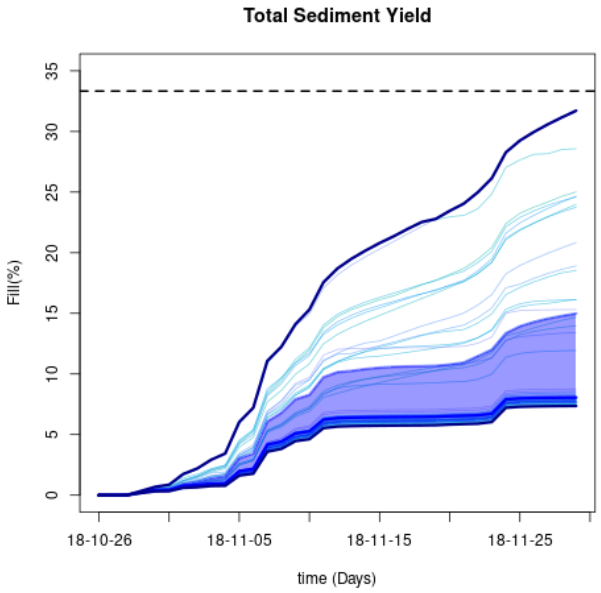

Figure 18: Functional boxplot of the Monte Carlo simulations of intense rain period at $\Delta = 35\,m$ resolution: distribution of time series of cumulated sediment yield at monitoring location (percentage of tank filling). The shaded area represents the second and third functional quartile of the resulting distribution, the darker lines the smallest and largest valued series. The horizontal dotted line represents the percentage of tank filling over one year resulting from the measurements described in [45].

the wide range of transients that can arise in long term simulations and to run even at high resolution with time step values that are dictated by accuracy rather than stability reasons, while guaranteeing mass conservation and positivity of the water and sediment layers.

The results obtained in the first verification and validation experiments confirm the efficiency, robustness and flexibility of the model. In particular, the model is able to reproduce transient high resolution features at a reduced computational cost and to reproduce correctly the main hydrographic features of the considered catchment. Furthermore, probabilistic forecasts can be carried out, also with limited computational effort, based on realizations of the soil data generated by the geostatistical preprocessor. Even though the model results are still far from full quantitative agreement with the available data, robust estimates of water levels, discharge and of the order of magnitude of the total sediment yield were achieved.

In future developments, the numerical model will be further integrated with its geostatistical counterpart, so as to reduce the computational cost of probabilistic simulation by application of multifidelity approaches, see e.g. [38]. Less elementary choices will be employed for the description of the many physical processes involved, in particular for the description of the infiltration process and the modelling of the bottom friction term. Implicit multirate time discretization approaches, see e.g. [9, 12], could contribute to further increase the computational efficiency of the model. It is also planned to improve the description of the subsurface flow, employing vertically averaged Darcy equations and coupling the subsurface flow to the surface flows along the lines proposed in several papers, see e.g. [14, 15, 22, 55]. Finally, also the local refinement techniques proposed in [16] for the same kind of numerical method employed here can be incorporated in the model, further enhancing its ability to resolve fine spatial features at a low computational cost.

Acknowledgements

The authors gratefully acknowledge the financial support of Fondazione Cariplo in the framework of the SMART-SED project, grant number 2017-0722. Many useful discussions with A. Radice are also kindly acknowledged, as well as the contributions by A. Abbate, J.K. Grudnicki and N. Togni to the preliminary phases of the development of this model.

References

[1] A. Abbate. Un modello numerico conservativo di erosione di versante. Master Thesis in Environmental Engineering, Politecnico di Milano, 2015.

[2] M.B. Abbott, J.C. Bathurst, J.A. Cunge, P.E. O'Connell, and J. Rasmussen. An introduction to the European Hydrological System—Systeme Hydrologique Europeen,"SHE", 1: History and philosophy of a physically-based, distributed modelling system. *Journal of Hydrology*, 87:45–59, 1986.

[3] M.B. Abbott, J.C. Bathurst, J.A. Cunge, P.E. O'Connell, and J. Rasmussen. An introduction to the European Hydrological System—Systeme Hydrologique Europeen,"SHE", 2: Structure of a physically-based, distributed modelling system. *Journal of Hydrology*, 87:61–77, 1986.

[4] J. Aitchison. The Statistical Analysis of Compositional Data. *Journal of the Royal Statistical Society: Series B*, 44:139–160, 1982.

[5] J.G. Arnold and J.R. Williams. Validation of SWRRB—simulator for water resources in rural basins. *Journal of Water Resources Planning and Management*, 113:243–256, 1987.

[6] R. Barnes, C. Lehman, and D. Mulla. Priority-flood: An optimal depression-filling and watershed-labeling algorithm for digital elevation models. *Computers & Geosciences*, 62:117–127, 2014.

[7] Richard Barnes. *RichDEM: Terrain Analysis Software*, 2016.

[8] G. A. Bemporad, J. Alterach, F. F. Amighetti, M. Peviani, and I. Saccardo. A distributed approach for sediment yield evaluation in Alpine regions. *Journal of Hydrology*, pages 370–392, 1997.

[9] L. Bonaventura, F. Casella, L. Delpopolo Carciopolo, and A. Ranade. A self adjusting multirate algorithm for robust time discretization of partial differential equations. *Computers and Mathematics with Applications*, 79:2086–2098, 2020.

[10] G. Büttner. CORINE land cover and land cover change products. In *Land use and land cover mapping in Europe*, pages 55–74. Springer, 2014.

[11] G. Büttner, J. Feranec, G. Jaffrain, L. Mari, G.Maucha, and T. Soukup. The CORINE land cover 2000 project. *EARSeL eProceedings*, 3:331–346, 2004.

[12] L. Delpopolo Carciopolo, L. Bonaventura, A. Scotti, and L. Formaggia. A conservative implicit multirate method for hyperbolic problems. *Computational Geosciences*, 23:647–664, 2019.

[13] V. Casulli. Semi-implicit finite difference methods for the two-dimensional shallow water equations. *Journal of Computational Physics*, 86:56–74, 1990.

[14] V. Casulli. A conservative semi-implicit method for coupled surface–subsurface flows in regional scale. *International Journal of Numerical Methods in Fluids*, 79:199–214, 2015.

[15] V. Casulli. A coupled surface-subsurface model for hydrostatic flows under saturated and variably saturated conditions. *International Journal of Numerical Methods in Fluids*, 85:449–464, 2017.

[16] V. Casulli. Computational grid, subgrid, and pixels. *International Journal of Numerical Methods in Fluids*, 90:140–155, 2019.

[17] V. Casulli and R.T. Cheng. Semi-implicit finite difference methods for three-dimensional shallow water flow. *International Journal of Numerical Methods in Fluids*, 15:629–648, 1992.

[18] H. Chanson. *The Hydraulics of Open Channel Flow: An Introduction. Physical Modelling of Hydraulics.* Butterworth-Heinemann, 1999.

[19] F.W. Chen and C.W. Liu. Estimation of the spatial rainfall distribution using inverse distance weighting (IDW) in the middle of Taiwan. *Paddy and Water Environment*, 10:209–222, 2012.

[20] M. Chiari and D. Rickenmann. The influence of form roughness on modelling sediment transport at steep slopes,. In *Proceedings of the International Conference on: Erosion and torrent control as a factor in sustainable river basin management.*, pages 25–28, 2007.

[21] L. Ciarapica and E. Todini. TOPKAPI: A model for the representation of the rainfall-runoff process at different scales. *Hydrological Processes*, 16:207–229, 2002.

[22] M. Discacciati, E. Miglio, and A. Quarteroni. Mathematical and numerical models for coupling surface and groundwater flows. *Applied Numerical Mathematics*, 43:57–74, 2002.

[23] C.O. Doten, L.C. Bowling, J.S. Lanini, E.P. Maurer, and D.P. Lettenmaier. A spatially distributed model for the dynamic prediction of sediment erosion and transport in mountainous forested watersheds. *Water Resources Research*, 42, 2006.

[24] N. Dragičević, B. Karleuša, and N. Ožanić. A review of the Gavrilović method (Erosion Potential Method) application. *Gradevinar: časopis Hrvatskog saveza gradevinskih inženjera*, 68:715, 2016.

[25] S. Dutta. Soil erosion, sediment yield and sedimentation of reservoir: a review. *Modeling Earth Systems and Environment*, 2:123, 2016.

[26] S. Endrizzi, S. Gruber, M. Dall'Amico, and R. Rigon. GEOtop 2.0: simulating the combined energy and water balance at and below the land surface accounting for soil freezing, snow cover and terrain effects. *Geoscientific Model Development*, 7:2831–2857, 2014.

[27] M. Davies et al. *The Standard Handbook for Aeronautical and Astronautical Engineers*. McGraw-Hill,, 2003.

[28] T. Day et al. *Degree-days: theory and application*. The Chartered Institution of Building Services Engineers, London, 2006.

[29] S. Fatichi, E.R. Vivoni, F. L. Ogden, V.Y. Ivanov, et al. An overview of current applications, challenges, and future trends in distributed process-based models in hydrology. *Journal of Hydrology*, 537:45–60, 2016.

[30] B. Fu, W.S. Merritt, B.F.W. Croke, T.R. Weber, and A.J. Jakeman. A review of catchment-scale water quality and erosion models and a synthesis of future prospects. *Environmental modelling & software*, 114:75–97, 2019.

[31] G. Garegnani, G. Rosatti, and L. Bonaventura. On the range of validity of the Exner-based models for mobile-bed river flow simulations. *Journal of Hydraulic Research*, 51:380–391, 2013.

[32] F. Gatti, A. Menafoglio, N. Togni, L. Bonaventura, D. Brambilla, M. Papini, and L. Longoni. A novel downscaling procedure for compositional data in the Aitchison geometry with application to soil texture data. *Stochastic Environmental Research and Risk Assessment*, 2020.

[33] Z. Gavrilović. *Inzenjering o bujicnim tokovima i eroziji*. Izgradnja, Beograd, 1972.

[34] Z. Gavrilović. Use of an empirical method(erosion potential method) for calculating sediment production and transportation in unstudied or torrential streams. In *International Conference on River Regime*, pages 411–422, Wallingford, 1988. Hydraulics Research Limited.

[35] L. Globevnik, D. Holjević, G. Petkovsek, and J. Rubinić. Applicability of the Gavrilović method in erosion calculation using spatial data manipulation techniques. In *Proceedings of the Symposium on: Erosion*

Prediction in Ungauged Basins, Integrating Methods and Techniques, pages 224–234. IAHS, 2003.

[36] E.S. Gross, L. Bonaventura, and G. Rosatti. Consistency with continuity in conservative advection schemes for free-surface models. *International Journal of Numerical Methods in Fluids*, 38:307–327, 2002.

[37] J.K. Grudnkici. Physically based numerical soil erosion model. Master Thesis in Civil Engineering for Risk Mitigation, Politecnico di Milano, 2018.

[38] O. Grujic, A. Menafoglio, G. Yang, and J. Caers. Cokriging for multivariate Hilbert space valued random fields: application to multi-fidelity computer code emulation. *Stochastic Environmental Research and Risk Assessment*, 32:1955–1971, 2018.

[39] G. Guennebaud, B. Jacob, et al. Eigen v3. http://eigen.tuxfamily.org, 2010.

[40] G.H. Hargreaves and R.G. Allen. History and evaluation of Hargreaves evapotranspiration equation. *Journal of Irrigation and Drainage Engineering*, 129:53–63, 2003.

[41] A. Hazen. Physical properties of sands and gravels with reference to use in filtration. *Report to Massachusetts State Board of Health*, 539, 1892.

[42] T. Hengl and J. De Jesuset al. SoilGrids250m: Global gridded soil information based on machine learning. *PLoS ONE*, 12:e0169748, 2017.

[43] S.B. Idso, R.D. Jackson, and R.J. Reginato. Remote-sensing of crop yields. *Science*, 196:19–25, 1977.

[44] V. Ivanov, A. Radice, M. Papini, and L. Longoni. Event-scale pebble mobility observed by rfid tracking in a pre-alpine stream: a field laboratory. *Earth Surface Processes and Landforms*, 45:535–547, 2020.

[45] V. I. Ivanov, D. Brambilla, L. Longoni, and M. Papini. Long term analysis of sediment transport in a Pre-Alpine river. In *Proceedings of the International Multidisciplinary Scientific GeoConference on Surveying Geology & Mining Ecology Management (SGEM), Vol. 3*, pages 171–178, 2016.

[46] D. Kershaw. The incomplete Cholesky conjugate gradient method for the iterative solution of systems of linear equations. *Journal of Computational Physics*, 26:43–65, 1978.

[47] A. Ketema and G.S. Dwarakish. Water erosion assessment methods: a review. *ISH Journal of Hydraulic Engineering*, pages 1–8, 2019.

[48] J.H. Kim. Spurious correlation between ratios with a common divisor. *Statistics and Probability Letters*, 44:383–386, 1999.

[49] R.J. LeVeque. *Numerical methods for conservation laws*. Springer, 1992.

[50] ARPA Lombardia. Portale dati idrologici arpa lombardia, 2021.

[51] J.A. Martín-Fernández, K. Hron, M. Templ, P. Filzmoser, and J. Palarea-Albaladejo. Model-based replacement of rounded zeros in compositional data: classical and robust approaches. *Computational Statistics & Data Analysis*, 56:2688–2704, 2012.

[52] J.A. Matthews. *Encyclopedia of Environmental Change*. Sage, 2013.

[53] W.S. Merritt, R.A. Letcher, and A. J. Jakeman. A review of erosion and sediment transport models. *Environmental Modelling & Software*, 18:761–799, 2003.

[54] C. Michel, V. Andréassian, and C. Perrin. Soil Conservation Service Curve Number method: How to mend a wrong soil moisture accounting procedure? *Water Resources Research*, 41, 2005.

[55] E. Miglio, A. Quarteroni, and F. Saleri. Coupling of free surface and groundwater flows. *Computers & Fluids*, 32:73–83, 2003.

[56] R.P.C. Morgan, J.N. Quinton, R.E. Smith, G. Govers, J.W.A. Poesen, K. Auerswald, G. Chisci, D. Torri, and M.E. Styczen. The European Soil Erosion Model (EUROSEM): a dynamic approach for predicting sediment transport from fields and small catchments. *Earth Surface Processes and Landforms*, 23:527–544, 1998.

[57] A. Pandey, S.K. Himanshu, S.K. Mishra, and V.P. Singh. Physically based soil erosion and sediment yield models revisited. *Catena*, 147:595–620, 2016.

[58] V. Pawlowsky-Glahn, J.J. Egozcue, and R. Tolosana-Delgado. *Modeling and analysis of compositional data*. John Wiley & Sons, 2015.

[59] F. Pedotti and F. Pomoni. Uso del database SoilGrids per il bacino del torrente Caldone. Bachelor Thesis in Civil and Environmental Engineering, Politecnico di Milano, 2020.

[60] V.M. Ponce and R.H. Hawkins. Runoff curve number: Has it reached maturity? *Journal of Hydrologic Engineering*, 1:11–19, 1996.

[61] K.G. Renard. *Predicting soil erosion by water: a guide to conservation planning with the Revised Universal Soil Loss Equation*

(RUSLE).Handbook. Number 703. Department of Agriculture, Science and Education Administration, 1997.

[62] D. Rickenmann. An alternative equation for the mean velocity in gravel-bed rivers and mountain torrents. *Hydraulic engineering*, 94:672–676, 1994.

[63] D. Rickenmann. Comparison of bed load transport in torrents and gravel bed streams. *Water Resources Research*, 37:3295–3305, 2001.

[64] R. Rigon, G. Bertoldi, and T.M. Over. GEOtop: A distributed hydrological model with coupled water and energy budgets. *Journal of Hydrometeorology*, 7:371–388, 2006.

[65] A.J.J. Van Rompaey, G. Verstraeten, K. Van Oost, G. Govers, and J. Poesen. Modelling mean annual sediment yield using a distributed approach. *Earth Surface Processes and Landforms*, 26:1221–1236, 2001.

[66] A.P.J. De Roo and V.G. Jetten. Calibrating and validating the LISEM model for two data sets from the Netherlands and South Africa. *CATENA*, 37:477–493, 1999.

[67] G. Rosatti, L. Bonaventura, A. Deponti, and G. Garegnani. An accurate and efficient semi-implicit method for section-averaged free-surface flow modelling. *International Journal of Numerical Methods in Fluids*, 65:448–473, 2011.

[68] G. Rosatti, R. Chemotti, and L. Bonaventura. High order interpolation methods for semi-Lagrangian models of mobile-bed hydrodynamics on Cartesian grids with cut cells. *International Journal of Numerical Methods in Fluids*, 47:1269–1275, 2005.

[69] S. Simoni, F. Zanotti, G. Bertoldi, and R. Rigon. Modelling the probability of occurrence of shallow landslides and channelized debris flows using GEOtop-FS. *Hydrological Processes*, 22:532–545, 2008.

[70] S. Sinclair and G.G.S. Pegram. A sensitivity assessment of the TOPKAPI model with an added infiltration module. *Journal of Hydrology*, 479:100–112, 2013.

[71] G. Smart and M. Jäggi. Sediment transport on steep slopes. Technical report, Mitteilung. 64. Versuchsanstalt für Wasserbau, Hydrologie und Glaziologie, ETH Zurich, 1983.

[72] A. Soares. Direct sequential simulation and cosimulation. *Mathematical Geology*, 33:911–926, 2001.

[73] B. Soto and F. Díaz Fierros. Runoff and soil erosion from areas of burnt scrub: comparison of experimental results with those predicted by the WEPP model. *CATENA*, 31:257–270, 1998.

[74] A. Stamm, N. Tarabelloni, A. Arribas Gil, F. Ieva, A. M. Paganoni, J. Romo, and F. Palma. ROAHD - Robust Analysis of High Dimensional Data, version 1.4.2. https://github.com/astamm/roahd, 2020.

[75] Y. Sun and M.G. Genton. Functional Boxplots. *Journal of Computational and Graphical Statistics*, 20:316–334, 2011.

[76] A. Veronelli and G. Messa. Uso degli RFID per il monitoraggio del trasporto solido nel torrente Caldone. Master Thesis in civil engineering for risk mitigation, Politecnico di Milano, 2019.

[77] N.R. Viney and M. Sivapalan. A conceptual model of sediment transport: application to the Avon River Basin in Western Australia. *Hydrological Processes*, 13:727–743, 1999.

[78] N.R. Viney, M. Sivapalan, and D. Deeley. A conceptual model of nutrient mobilisation and transport applicable at large catchment scales. *Journal of Hydrology*, 240:23–44, 2000.

[79] J.M. Wicks and J.C. Bathurst. SHESED: a physically based, distributed erosion and sediment yield component for the SHE hydrological modelling system. *Journal of Hydrology*, 175:213–238, 1996.

[80] M.S. Wigmosta, L.W. Vail, and D.P. Lettenmaier. A distributed hydrology-vegetation model for complex terrain. *Water Resources Research*, 30:1665–1679, 1994.

[81] J.R. Williams, A.D. Nicks, and J.G. Arnold. Simulator for water resources in rural basins. *Journal of Hydraulic Engineering*, 111:970–986, 1985.

[82] W.H. Wischmeier and D.D. Smith. *Predicting rainfall erosion losses: a guide to conservation planning.* Handbook. Number 537. Department of Agriculture, Science and Education Administration, 1978.

[83] R.A. Young, C.A. Onstad, D.D. Bosch, and W.P. Anderson. AGNPS: A nonpoint-source pollution model for evaluating agricultural watersheds. *Journal of soil and water conservation*, 44:168–173, 1989.

[84] G. Zhang, Y. Liu, Y. Han, and X.C. Zhang. Sediment transport and soil detachment on steep slopes: I. Transport capacity estimation. *Soil Science Society of America Journal*, 73:1291–1297, 2009.

MOX Technical Reports, last issues

Dipartimento di Matematica
Politecnico di Milano, Via Bonardi 9 - 20133 Milano (Italy)

31/2021 Ferraccioli, F.; Arnone, E.; Finos, L.; Ramsay, J.O.; Sangalli, L.M.
Nonparametric density estimation over complicated domains

32/2021 Sangalli, L.M.
Spatial regression with partial differential equation regularization

33/2021 Lupo Pasini, M.; Gabbi, V.; Yin, J.; Perotto, S.; Laanait, N.
Scalable balanced training of conditional generative adversarial neural networks on image data

30/2021 Fumagalli, I.
A reduced 3D-0D FSI model of the aortic valve including leaflets curvature

29/2021 Fumagalli, I.; Vitullo, P.; Scrofani, R.; Vergara, C.
Image-based computational hemodynamics analysis of systolic obstruction in hypertrophic cardiomyopathy

28/2021 Ferro, N.; Perotto, S.; Bianchi, D.; Ferrante, R.; Mannisi, M.
Design of cellular materials for multiscale topology optimization: application to patient-specific orthopedic devices

26/2021 Vigano, L.; Sollini, M.; Ieva, F.; Fiz, F.; Torzilli, G.
Chemotherapy-Associated Liver Injuries: Unmet Needs and New Insights for Surgical Oncologists

27/2021 Scimone, R.; Menafoglio, A.; Sangalli, L.M.; Secchi, P.
A look at the spatio-temporal mortality patterns in Italy during the COVID-19 pandemic through the lens of mortality densities

24/2021 Regazzoni, F.; Chapelle, D.; Moireau, P.
Combining Data Assimilation and Machine Learning to build data-driven models for unknown long time dynamics - Applications in cardiovascular modeling

25/2021 Tenderini, R.; Pagani, S.; Quarteroni, A.; Deparis S.
PDE-aware deep learning for inverse problems in cardiac electrophysiology